

Three-dimensional imaging of liquid crystal structures and defects by means of holographic manipulation of colloidal nanowires with faceted sidewalls†

David Engström,^{ab} Rahul P. Trivedi,^{ac} Martin Persson,^{ab} Mattias Goksör,^b Kris A. Bertness^d and Ivan I. Smalyukh^{*ace}

Received 1st February 2011, Accepted 27th April 2011

DOI: 10.1039/c1sm05170a

We use nanowires with faceted sidewalls for mapping of the patterns of three-dimensional orientational order and defect structures. In chiral nematics, the nanowires follow the local average orientation of rod-shaped molecules. When spatially translated by use of holographic optical tweezers in three dimensions, they mediate direct nondestructive visualization of the helicoidal ground-state structures, edge and screw dislocations, and kinks, as well as enable non-contact manipulation of these defects. We probe interactions of faceted nanowires with different defects and demonstrate their spontaneous self-alignment along the cores of singular defect lines.

1. Introduction

Defect structure and dynamics often determine material properties and their practical applications,^{1–13} being also critically important for fundamental phenomena ranging from super-solidity to phase transitions, and to early universe cosmic strings. Edge and screw dislocations are common defects in the long-range or quasi long-range translational ordering of solid crystals and a number of soft materials such as cholesteric liquid crystal (CLC) fluids. Colloidal crystals and anisotropic fluids such as CLCs are routinely used as model systems to provide insights into the defect-related processes occurring on the length scales ranging from atomic to cosmic.^{1,4,5,10–18} Simultaneous direct three-dimensional (3D) structural characterization and non-contact control of the defects are in a great demand but rarely achievable at the level of individual defects.^{13–20}

In this work, we use holographic optical tweezers²¹ to manipulate GaN nanowires²² in CLCs and locally probe spatial patterns of 3D orientational order and core structure of defects such as dislocations. CLCs have a twisted ground state with helical configuration of the director \mathbf{n} , a unit vector with non-polar symmetry ($\mathbf{n} \equiv -\mathbf{n}$) that specifies the local average

orientation of the anisotropic constituent molecules. CLCs with short pitch p (distance along the helical axis corresponding to twist of \mathbf{n} by 2π) have elastic properties of lamellar phases with $p/2$ being the thickness of an elementary “lamella.” Dislocations frequently appear in CLCs as a result of temperature quenching from the isotropic phase, applied fields, and surface boundary conditions. The used nanowires are visible in a regular optical microscope and provide a direct visualization of the local average orientation of the surrounding liquid crystal molecules and \mathbf{n} when placed into the CLC regions of interest (such as dislocations) by use of the non-contact optical manipulation. Further, the elasticity-mediated self-alignment of optically manipulated nanowires with \mathbf{n} allow for the non-contact control and 3D visualization of CLC structures and defects. We also observe that the used nanowires with faceted sidewalls self-align and spontaneously assemble into singular cores of disclinations, with the faceted sidewalls being parallel to the line singularities; this may provide novel means of fabrication of CLC-based nanocomposites of interest for a number of new photonic, meta-material, and electro-optic applications.²³

2. Experimental

2.1. Materials and sample preparation

The CLC mixtures were formed by mixing nematic hosts E7, ZLI-3412, or ZLI-2806 with the chiral agent CB15. The refractive index and elastic properties of the used materials are provided in Table 1. For the fluorescence confocal polarizing microscopy (FCPM) imaging, the samples were doped with 0.01 wt% of the fluorescent dye n,n' -bis(2,5-di-*tert*-butylphenyl)-3,4,9,10-perylene-dicarboximide (Aldrich²⁴) giving strong polarized fluorescence signals without changing the CLC structure and properties.²⁰ We use GaN nanowires with a hexagonal

^aDepartment of Physics, University of Colorado, Boulder, Colorado, 80309, USA. E-mail: Ivan.Smalyukh@colorado.edu

^bDepartment of Physics, University of Gothenburg, 412 96 Göteborg, Sweden

^cLiquid Crystal Materials Research Center, University of Colorado, Boulder, Colorado, 80309, USA

^dNational Institute of Standards and Technology, Boulder, Colorado, 80305, USA

^eRenewable and Sustainable Energy Institute, University of Colorado, Boulder, Colorado, 80309, USA

† Electronic supplementary information (ESI) available: Additional information on growth of nanowires, and four videos. See DOI: 10.1039/c1sm05170a

Table 1 Material parameters of the used nematic hosts and chiral additives

Material/property	K_{11}/pN	K_{22}/pN	K_{33}/pN	Δn	H_{HTP} of CB-15/ μm^{-1}
E7 (from EM Chemicals)	10.4	7.4	16.6	0.22	7.3
ZLI-3412 (from EM Chemicals)	14.1	6.7	15.5	0.078	6.3
ZLI-2806 (from EM Chemicals)	14.9	7.9	15.4	0.045	6.1

cross-section having ~ 150 nm wide sides and length-width aspect ratios ~ 30 (Fig. 1a). These nanowires were grown^{22,24} on thin AlN buffer layers on Si(111) substrates by molecular beam epitaxy under conditions of high substrate temperature (810–830 °C) and high nitrogen plasma flux at a chamber pressure of ~ 2.6 mPa. Under these growth conditions, the nanowires nucleate spontaneously. The growth rates were from 0.1 to $0.2 \mu\text{m h}^{-1}$. The used nanowires were Si-doped and had an absorption coefficient of $\sim 80 \text{ cm}^{-1}$ at 1064 nm, which causes only

negligible heating of the surrounding LC when the nanoparticles are manipulated. The long axis of the nanowires follows the c -axis (0001) of their wurtzite crystal structure, with the sidewalls all being m -planes [$(1\bar{1}00)$ family], and thus they are hexagonal in cross-section. The $\sim 10 \mu\text{m}$ long GaN rods with ~ 150 nm sides of the hexagonal cross-section were first dispersed in isopropanol and then transferred into the CLC by solvent exchange. Typically, $\sim 10 \mu\text{L}$ of isopropanol containing nanowires was stirred with $\sim 60 \mu\text{L}$ of CLC after which the vial was left for ~ 10 hours

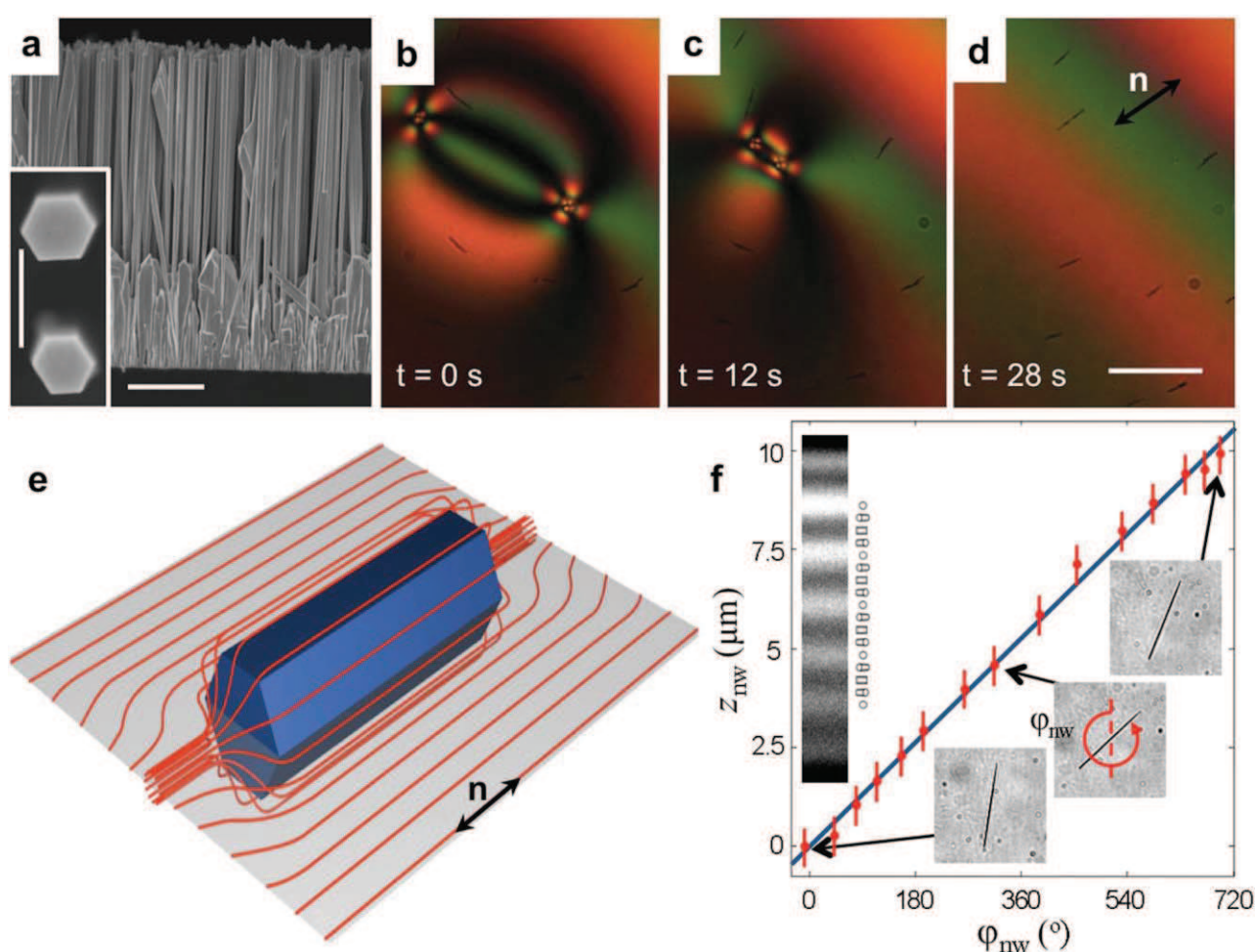


Fig. 1 Nanowires as nanoscale probes of the long-range molecular alignment in LCs. (a) SEM micrographs showing GaN nanowires as grown on a thin AlN buffer layer on a Si(111) substrate; the scale bar is $5 \mu\text{m}$. The inset in (a) shows that the nanowires have hexagonal cross-sections; the scale bar is 500 nm. (b, c and d) Polarizing optical microscopy images showing that orientations of nanowires (having appearance of $4\text{--}10 \mu\text{m}$ dark lines) provide visualization of temporal evolution of $\mathbf{n}(\mathbf{r})$ as nematic defects annihilate; the elapsed time is marked on the images; the scale bar is $50 \mu\text{m}$. The colors result from interference of polarized light passing through the sample of slightly varying thickness. (e) Schematic of the structure around the GaN nanowires in the LC with the uniformly aligned far-field director. (f) Vertical position z_{nw} along the helix is a linear function of ϕ_{nw} visualizing the helicoidal $\mathbf{n}(\mathbf{r})$ (solid line); the reading error of $\pm 0.5 \mu\text{m}$ is shown by error bars. The insets show (left) FCPM vertical cross-section and schematics of the uniform cholesteric structure and (right) representative images corresponding to different vertical positions of a nanowire.

to evaporate the isopropanol at $\sim 40^\circ\text{C}$ on a hotplate. The final mixture consisting of dye-doped CLC and rods was stirred just before the CLC cell preparation to improve the quality of dispersion. FCPM and polarizing microscopy textures show that the GaN nanowire exerts tangential surface boundary conditions on the liquid crystal director, aligns parallel to it, and minor additional local director distortions appear only at the rod's ends (Fig. 1b and e) while the studied structures and defects remain unperturbed.

To promote appearance of dislocations in cholesteric lamellae, wedge CLC cells with a small dihedral angle $\alpha < 2^\circ$ and planar cholesteric structure were fabricated by use of 0.15 mm thick glass plates. The substrates were spin-coated with $\sim 1\text{ wt}\%$ solution of poly-vinyl-alcohol (PVA) in deionized water at 5000 rpm followed by baking in an oven for 1 h at 100°C . Two types of cells were used: for some cells the PVA-coated substrates were assembled with no further treatment, while for the most cells the PVA-coated substrates were unidirectionally rubbed with a velvet cloth to force the liquid crystal molecules to align parallel to the rubbing direction. Wedge-shaped cells were prepared by using 80 μm spacers on one edge of the cell and no spacers on the opposite edge. The cells were then filled with a liquid crystal and sealed with epoxy. The confinement of the CLC into the wedge-shaped cells promoted facile appearance of defects such as dislocations and disclinations, which we have imaged by means of FCPM and classified according to the scheme of Kleman and Friedel.¹⁶ In the so-called λ -disclinations, the material \mathbf{n} -director field is non-singular because of \mathbf{n} being parallel to the defect line in its core, so that the singularity is observed only in the immaterial director fields of CLC helical axis χ and τ orthogonal to both \mathbf{n} and χ . In the τ -disclinations, the τ -field is non-singular but \mathbf{n} and χ director fields are singular. In χ -disclinations, the singularities are found in \mathbf{n} and τ director fields but not in the χ -field.

2.2. Integrated optical setup for imaging and manipulation

To manipulate nanowires, we have utilized holographic optical tweezers (HOT).^{15,25} In the HOT setup (Fig. 2), a collimated 5 mm beam from a linearly polarized Ytterbium-doped fiber laser (IPG Photonics, $\lambda = 1064\text{ nm}$) is resized by a telescope to slightly overfill the active area of the phase-only spatial light modulator (Boulder Nonlinear Systems). We have used laser trap powers of 35–250 mW, smaller than the CLC realignment threshold. After being reflected off the SLM, the beam is coupled into the back aperture of a $60\times$ oil-immersion microscope objective (NA = 1.42, $\sim 60\%$ transmission at 1064 nm) by using a second telescope. The second telescope (in the so-called 4-f arrangement) also images the phase profile encoded by the SLM to the back focal plane of the microscope objective. The holograms displayed on the SLM create trap patterns in the focal plane of the microscope objective. A dichroic mirror (Chroma) reflects the trapping laser beam into the microscope objective while transmits visible light used for imaging. By displaying holograms on the SLM, the phase of the reflected light is controlled between 0 and 2π at each pixel. In total the SLM has 512×512 pixels, each of size $15 \times 15\ \mu\text{m}^2$. New holograms can be displayed on the SLM at a rate of 10–30 Hz. The positions of the traps defined by the calculated holograms are controlled by HOT software (Arryx, Inc.). Bright-field imaging with visible light is performed using a charge-coupled device (CCD) camera (Ptegrey, Flea 2, IEEE 1394b). A half-wave plate is used to control the beam's linear polarization direction. The spatial positions of traps are computer-controlled and optical manipulation of GaN nanowires is achieved by using one or two traps positioned at the ends of a nanowire.

The HOT setup is integrated with an inverted optical microscope (IX-81, Olympus) and is capable of working in parallel with imaging in a regular brightfield mode and in the FCPM imaging mode enabled by the confocal scanning unit FV300

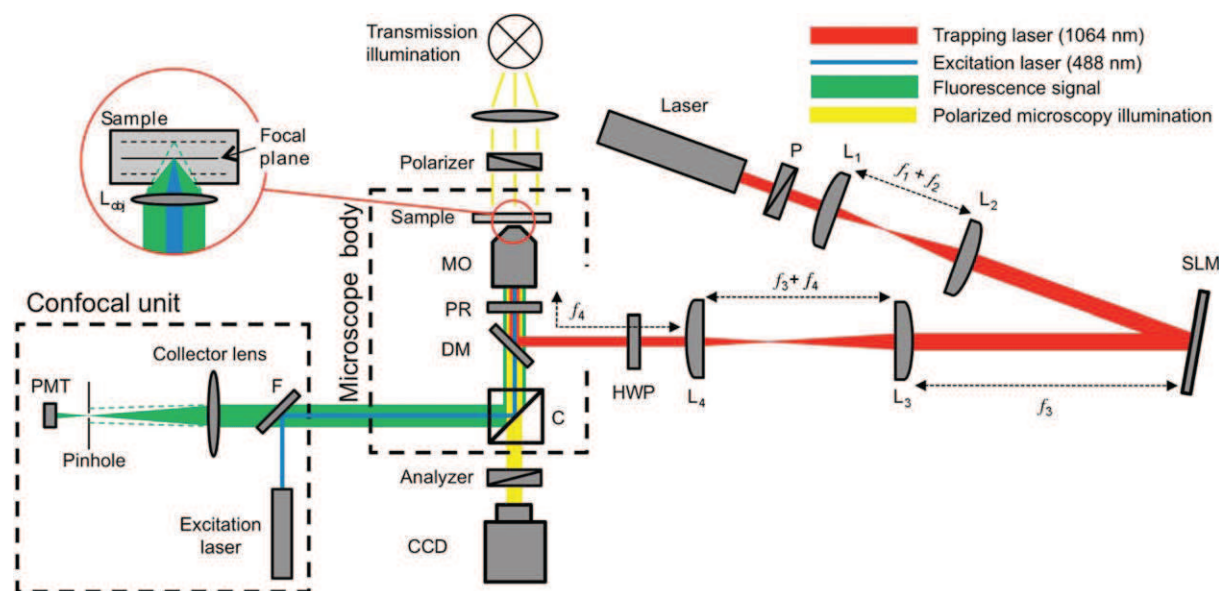


Fig. 2 Schematic of integrated HOT and FCPM setup. L_1 ($f_1 = 100\text{ mm}$), L_2 ($f_2 = 250\text{ mm}$), L_3 ($f_3 = 850\text{ mm}$), and L_4 ($f_4 = 400\text{ mm}$) are plano-convex lenses with antireflection coating for 1064 nm. P is a Glan-Laser polarizer for 1064 nm; SLM is the spatial light modulator; HWP is a half-wave retarder plate; DM is the dichroic mirror; MO is the microscope objective; C is a beam-splitting cube; F is a dichroic filter; PMT is a photomultiplier tube. L_{obj} represents the effective lens in the microscope objective.

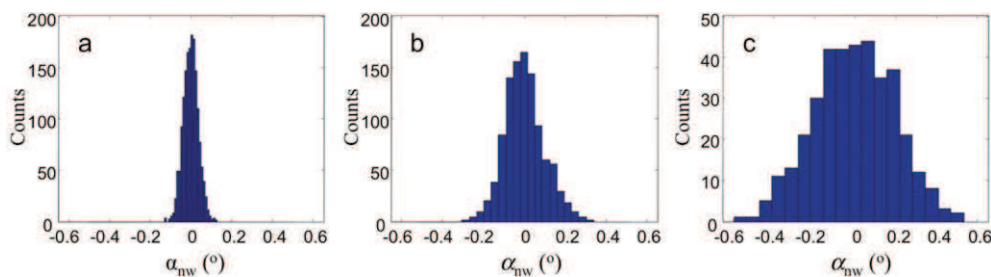


Fig. 3 Angular distributions of orientations for a nanowire due to thermal fluctuations around the equilibrium orientation (a) in a nematic, (b) in the CLC of equilibrium pitch $p = 50 \mu\text{m}$, and (c), in the CLC with a pitch of $p = 5 \mu\text{m}$. The distribution data were obtained by use of the particle tracking video microscopy (see, for example, ref. 23).

(Olympus).^{15,23,25} In the FCPM imaging mode, the linearly polarized excitation beam (488 nm Ar laser) is focused by the $60\times$ oil-immersion objective to a small ($<1 \mu\text{m}^3$) volume within the sample. This 3D orientational imaging is based on the use of anisotropic dye molecules and linearly polarized excitation and detection. The FCPM technique links the orientation of \mathbf{n} to the intensity of the measured fluorescent signal.^{16,20} The fluorescence intensity in the FCPM images depends on the angle γ between the linearly polarized excitation light and the dye transition dipole following \mathbf{n} , according to $I_{\text{FCPM}} \approx \cos^4 \gamma$.¹⁶ For the FCPM probing light polarization along the y -axis (orthogonal to the image plane), the maximum-intensity stripes in the images correspond to \mathbf{n} being along the y -axis. FCPM provides independent means of 3D imaging that we use for a comparative analysis of the CLC director structures and defects visualized by optically manipulated nanowires.

3. Results and discussion

In a liquid crystal, GaN nanowires spontaneously orient with their faceted sidewalls along \mathbf{n} and provide visualization of the spatio-temporal changes of the director field $\mathbf{n}(\mathbf{r}, t)$, such as those

due to annihilation of defects after cooling the sample from isotropic to nematic phase (Fig. 1a–d). This alignment is enforced by the medium's elasticity favoring the orientation of rod-like inclusions along \mathbf{n} . Because of the tangential boundary conditions, \mathbf{n} is parallel to the six large-area side faces of the hexagonal nanowire (Fig. 1e), so that the elastic energy due to the particle-induced elastic distortions is minimized. Assuming that the Frank elastic constants for splay (K_{11}), twist (K_{22}), and bend (K_{33}) are equal to the average elastic constant $K = (K_{11} + K_{22} + K_{33})/3$, the free energy cost of rod realignment from its equilibrium orientation ($\theta = 0$) to an angle θ can be estimated as that for a cylinder of radius R circumscribing the hexagon's edges $\Delta F_{\text{elastic}} \approx 2\pi K \theta^2 L / \ln [2L/R]$.²⁶ For typical nanowire dimensions and $K \approx 10 \text{ pN}$ (Table 1), one finds $\Delta F_{\text{elastic}} \approx 10^{-16} \theta^2 \text{ J}$. Therefore, thermally driven angular fluctuations in a nematic host are elasticity-suppressed so that θ is less than 0.5° , in agreement with the experimental Gaussian distribution of nanowire orientations (Fig. 3a). This confirms that the physics of the self-alignment of the nanowires due to the elastic properties of the liquid crystal is reminiscent to that reported in the pioneering work of de Gennes and Brochard²⁶ and several early experimental works^{27,28} that focused on the use of ferromagnetic

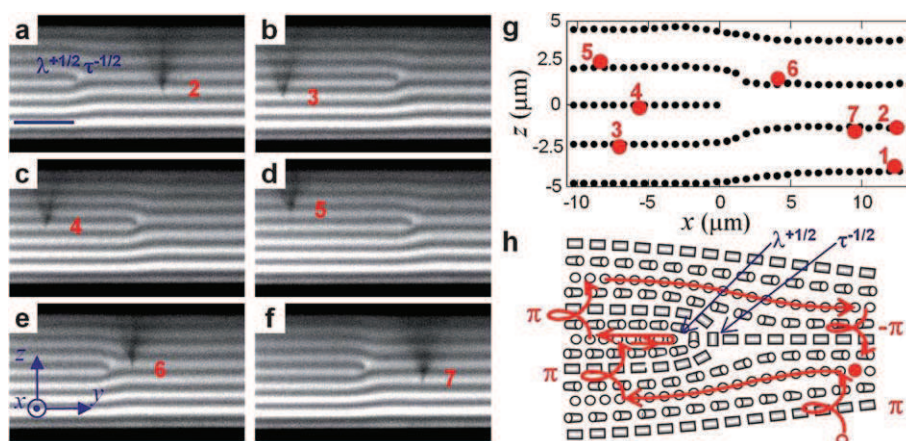


Fig. 4 Direct probing of the Burgers vector and core structure of a dislocation. (a–f) Confocal vertical cross-sections (obtained for the FCPM probing light polarization orthogonal to the images) showing sequential translation of the nanowire along a Burgers circuit containing points 2–7 in (a–f): (a) starting at the point #2, (b) the nanowire was continuously translated beneath the dislocation to the location #3 and then (c) rotated 180° CCW with the corresponding translational shift upward for one cholesteric layer; pushing the nanowire to the right on the image revealed that the layer is discontinuous as the dislocation resisted the nanowire motion; (d) the rod was rotated 180° CCW again while shifting one layer upward; (e) the nanowire was moved above the dislocation to the position #6 and then (f) rotated 180° CW while shifting one layer downward and closing the Burgers circuit. The scale bar in (a) is $10 \mu\text{m}$. (g) Layers displacement around the edge dislocation obtained from FCPM images (black dots) and nanowire positions corresponding to (a–f) shown by red filled circles. (h) Schematics of the reconstructed core structure of the $b = p/2$ dislocation with the Burgers circuit and nanowire trajectory (red).

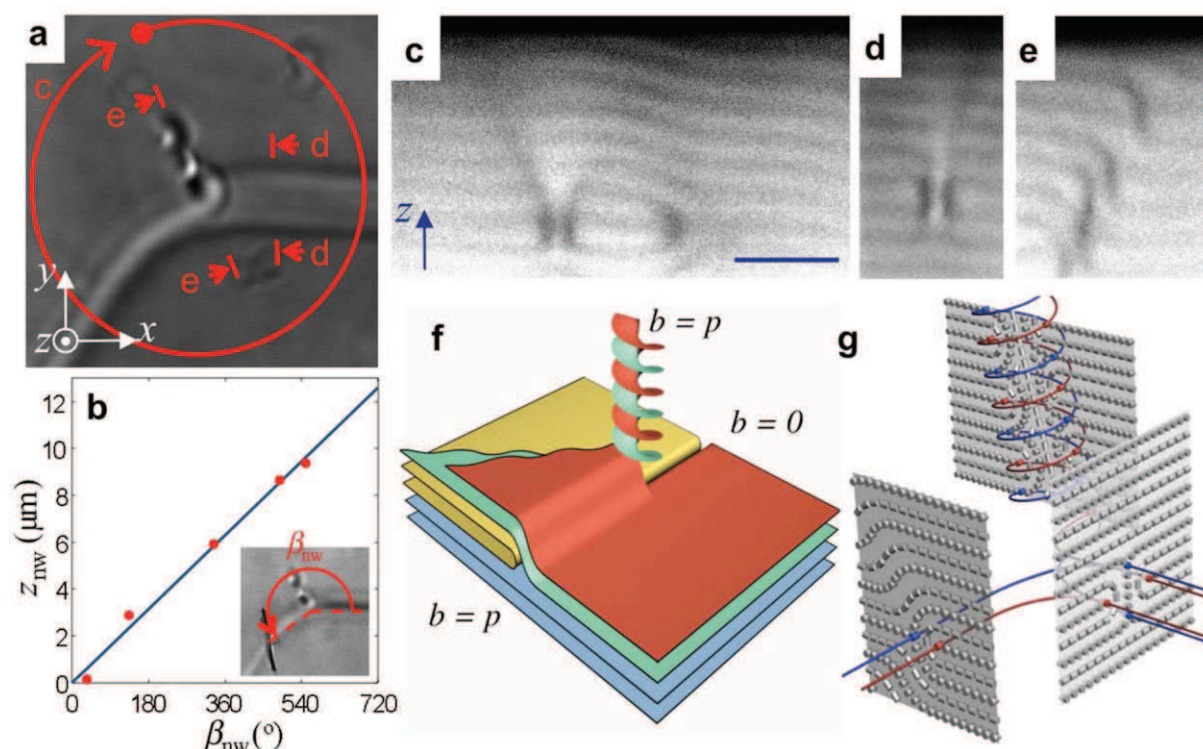


Fig. 5 Probing the Burgers vector conservation at a node of defects. (a) A node of screw and edge dislocations and an elementary oily streak; the screw dislocation extends between the cell surface and the node. (b) Vertical position of the nanowire as a function of the nanowire's in-plane angular position β_{nw} [marked in the inset of (b)]. The nanowire was kept oriented along the y -axis and moved around the screw dislocation by varying its angular position β_{nw} . (c–e) FCPM vertical cross-sections obtained for the polarization parallel to the y -axis along the (c) circular trajectory and (d and e) straight lines marked in (a). The scale bar in (c) is 10 μm . (f) A model of the observed node of defects in the layered structure with the Burgers vector values marked next to the defect lines. (g) Schematics of the molecular alignment with the nonsingular λ -disclinations in the defect cores forming dipolar structures in the core of dislocations and a quadrupole of λ -disclinations in the core of an elementary oily streak.

rod-shaped or needle-shaped nanoparticles aligning with the director to enhance the response to external magnetic fields. Similarly, elasticity-mediated alignment of nanorods in CLCs with optically tunable cholesteric pitch allowed for achieving rotation of colloidal rods by means of optical illumination.²⁹ In contrast to these studies, rather than exerting torques on the liquid crystal host by rotating rod-like particles or exerting torques on such particles by means of rotating \mathbf{n} as in ref. 27–29, we use holographic optical tweezers to translate GaN nanowires in 3D without significantly perturbing \mathbf{n} or equilibrium orientation of the nanowire. This non-contact spatial translation of the nanowire probe mechanically coupled to the orientation of \mathbf{n} allows us to map the complex 3D patterns of the director field that would be impossible to decipher by use of colloidal probes without such 3D manipulation.³⁰

An important property of the studied faceted colloidal inclusions in the liquid crystal host is that the only minimal local elastic distortions of \mathbf{n} appear at the ends of the nanowire (Fig. 1e). This is a natural result as the lateral size of the used nanowires is comparable to the so-called surface anchoring extrapolation length $l_e = K/W_p > R$, where $W_p \approx 10^{-5} \text{ J m}^{-2}$ is the estimated polar surface anchoring coefficient. Therefore, the competition between the surface anchoring and bulk elastic energies favors minimum bulk elastic distortions at the nanowire ends while adopting the equilibrium orientation of the nanowire along \mathbf{n} . Consistent with this analysis, bright-field transmission-

mode optical microscopy (typically used to mediate visualization of liquid crystal defects based on light scattering^{15–18,23}) and FCPM imaging reveal no point or line singularities in the liquid crystal bulk next to the colloid or at the interface of liquid crystal and the nanowire. We point out, however, that surface point defects such as the so-called “boojums” and other defects may be induced by colloids of similar shape but with larger transverse size or stronger tangential or vertical surface anchoring. Because of the submicron lateral size, weak surface anchoring, and the large length-to-width aspect ratio, the GaN colloidal inclusions exhibit equilibrium alignment and weak elastic distortions in the surrounding liquid crystal that are very different from those due to polygonal platelet particles (including hexagonal platelets),²³ although the common feature is that the large-area faces align parallel to \mathbf{n} in both cases. Furthermore, despite the fact that the transverse size of GaN nanowires is comparable to the size of 150–500 nm spherical colloids with strong vertical boundary conditions studied by Škarabot and Mušević (that induce strong elastic distortions),³¹ the weak tangential boundary conditions enable minimum-distortion director configuration shown in Fig. 1e. This is consistent with the other known literature examples demonstrating that spherical and cylindrical colloids can induce strong or weak distortions of the surrounding director field depending not only on the size and shape of colloids, but also on the strength and type of the surface anchoring boundary conditions.^{26–37}

When dispersed in CLCs, the nanowires orient along $\mathbf{n}(\mathbf{r})$ of the equilibrium helicoidal structure (Fig. 1f). As the cholesteric pitch decreases from infinity (nematic) to the used relatively short pitch values of $5\ \mu\text{m}$ with the addition of the chiral dopant (Table 1), the angular distribution of nanowire orientations broadens (Fig. 3), although the width of the distribution remains a fraction of degree even for the CLC with $p = 5\ \mu\text{m}$. The reason for the distribution broadening is likely that the transverse size R of the nanowire corresponds to a certain angular twist of the equilibrium helicoidal structure of the CLC ($360R/p$, ~ 10 degrees for $p = 5\ \mu\text{m}$). This results in a weaker elastic suppression of the angular thermal fluctuations of the nanowire in the CLC matrix as compared to the case of the nematic, although the colloidal nanowire still aligns parallel to the local $\mathbf{n}(\mathbf{r})$ corresponding to the center of the nanowire.

We control and probe 3D nanowire orientations and positions in the CLC by use of a combination of holographic optical tweezers working at $\lambda = 1064\ \text{nm}$, optical transmission microscopy, and a stepper motor controlling the sample's vertical position relative to the focal plane of an objective with 10 nm precision. For optical manipulation, one or two laser traps are positioned at the ends of a nanowire and then used to rotate and move it in 3D. In CLCs, nanowire orientation and position along the helical axis are coupled to each other: translation across the "cholesteric layers" is possible only *via* rotation following the helicoidal $\mathbf{n}(\mathbf{r})$ (Fig. 1f and Video S1†). The handedness of the helix and the rotation direction determine whether the nanowire moves upward or downward; its translation away from the microscope objective is typically easier than toward it, due to the scattering forces originating from the large nanowire-CLC refractive index mismatch. The measured vertical position z_{nw} of a nanowire along the helix is a linear function of its in-plane orientation angle ϕ_{nw} (Fig. 1f), consistent with the $\mathbf{n}(\mathbf{r})$ of the equilibrium helicoidal structure $\mathbf{n}(z) = \{\cos(2\pi z/p), \sin(2\pi z/p), 0\}$. From the linear fit of the experimental data shown in Fig. 1f by $z_{\text{nw}} = \phi_{\text{nw}} p/(2\pi)$, the measured effective pitch is $p = 5.3 \pm 0.3\ \mu\text{m}$, matching that obtained from the FCPM cross-section in the same location (top left inset of Fig. 1f).

In order to apply our technique to imaging of complex 3D director structures and defects, we have constructed wedge cholesteric cells with a dihedral angle about 2° and strong surface anchoring that keeps near-surface cholesteric layers parallel to substrates. Elementary edge dislocations perpendicular to the direction of the thickness gradient introduce additional cholesteric lamellae, in accord with increasing thickness of the wedge (Fig. 4). These dislocations have their cores split into disclination pairs and are often accompanied by other cholesteric defects, forming complex 3D configurations of $\mathbf{n}(\mathbf{r})$.

Although the non-destructive 3D imaging of $\mathbf{n}(\mathbf{r})$ around defects can be achieved by means of holographically manipulated nanowires alone, we use FCPM imaging for the comparative analysis of nanowire positions and orientations relative to $\mathbf{n}(\mathbf{r})$. In the vertical FCPM cross-sections, the nanowires oriented orthogonally to the confocal image give rise to a dark triangular-wedge spreading upward from the position of the rod (Fig. 4a–f), which is due to the scattering of the FCPM excitation light by the high-index GaN nanowire ($n_{\text{GaN}} = 2.4$, much larger than the effective CLC indices within 1.5–1.7). Optical translation of a nanowire serves as a single-particle probe of $\mathbf{n}(\mathbf{r})$, allowing one

not only to measure the equilibrium pitch but also to map changes in its effective value due to defects, yielding results that are in agreement with FCPM imaging (Fig. 4). The confocal vertical cross-sections in Fig. 4 show sequential translation of the nanowire along a Burgers circuit with the translation across the cholesteric layers implemented by rotating the nanowire. The attempted optical translation of a nanowire across the dislocation (discontinuity) in a layered CLC structure results in stretching of the dislocation resisted by its line tension (for example, when moving the nanowire from point #4 in Fig. 4c to the right we observe that as the dislocation eventually moves to the right and stretches when the nanowire approaches the defect core). A combination of rotational and translational motion along the so-called Burgers circuit (Fig. 4) reveals the Burgers vector's magnitude $|\mathbf{b}| = b = p/2$ and that the dislocation core is split into the so-called λ - and τ -disclinations forming a $\lambda^{+1/2}\tau^{-1/2}$ pair (Fig. 4h).³⁰ Furthermore, for a fixed nanowire orientation, optical translation of the nanowire provides direct visualization of the CLC layer displacements and the layered structures (Fig. 4g). As the nanowire is translated at a constant orientation within curved cholesteric layers displaced upward or downward with respect to the flat orientation parallel to the confining glass plates (*i.e.*, due to the dislocation defects), the nanowire shifts

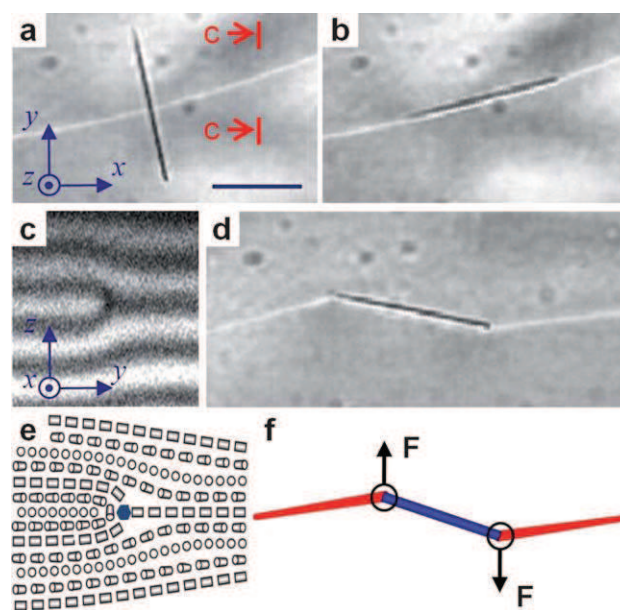


Fig. 6 Self-alignment and self-positioning of a nanowire in the core of an edge dislocation. (a) A nanowire positioned orthogonally to the dislocation; the scale bar is $5\ \mu\text{m}$. (b) The nanowire escapes from the laser traps and self-rotates to become co-localized with the singular τ -disclination. (c) Defect core structure visualized by the FCPM vertical cross-section along the c - c line marked in (a) and obtained for FCPM polarization orthogonal to the image. (d) Two optical traps moving in opposite directions rotate the nanowire, allowing one to manipulate the defect line that follows the nanowire orientation. (e) Schematics of the core structure of the studied $b = p/2$ dislocation with the nanowire self-positioned in the core of the singular τ -disclination. (f) Schematics of the defect manipulation by the means of a nanowire pinned to the defect core shown in (d); the optical trapping forces (F) in opposite directions orthogonal to the initial orientation of the defect line are exerted at the nanowire ends.

upward or downward in accord with the displacement of the layers to preserve its orientation parallel to the local $\mathbf{n}(\mathbf{r})$. Therefore, one can probe layer displacements by directly measuring the relative vertical position of the nanowire by means of a combination of bright-field optical imaging and holographic positioning of the nanowire or, alternatively, by vertical translation of infinity-corrected objective with a piezo-drive (Fig. 4). The reconstructed layer profiles (Fig. 4g) match those obtained from the FCPM images (Fig. 4a–f) and are consistent with the layer displacement field around a dislocation in a lamellar liquid crystal predicted by the nonlinear elastic theory.³⁸ Importantly, the complete 3D structure in the vertical cross-section of the sample can be deduced from regular brightfield images similar to those shown in the insets of Fig. 1f and is generally consistent with the results of FCPM imaging (Fig. 4a–f).

We have also probed a screw dislocation that forms a node with an edge dislocation and an elementary oily streak (Fig. 5).³⁹ A nanowire was moved around the screw dislocation while keeping its in-plane orientation constant (Fig. 5a and b). The measured change of the vertical z -position along the helix reveals

that the Burgers vector of the screw dislocation is $b = p$. Furthermore, similar nanowire-assisted probing of the other defects connected at the node reveals that the total Burgers vector at the node is conserved as the $b = p$ screw dislocation is connected to a $b = p$ edge dislocation and an elementary oily streak of $b = 0$ (Fig. 5). An interesting feature of these interconnected defects is that their cores are split into nonsingular λ -disclinations of opposite signs forming dipoles in cores of dislocations and a quadrupole in the core of an elementary oily streak. The disclinations smoothly transform between the cores of the defects (Fig. 5g).

Several recent studies have demonstrated that colloidal inclusions in liquid crystals can interact with defects to minimize free energy,^{33–36} although these effects have been explored mostly only for spherical and cylindrical colloids. We have studied interactions between the nanowires with faceted sidewall surfaces and CLC defects and observe that the strength and nature of these interactions strongly depend on whether the defect core is singular or nonsingular. To demonstrate this, we use a $b = p/2$ dislocation having both singular and

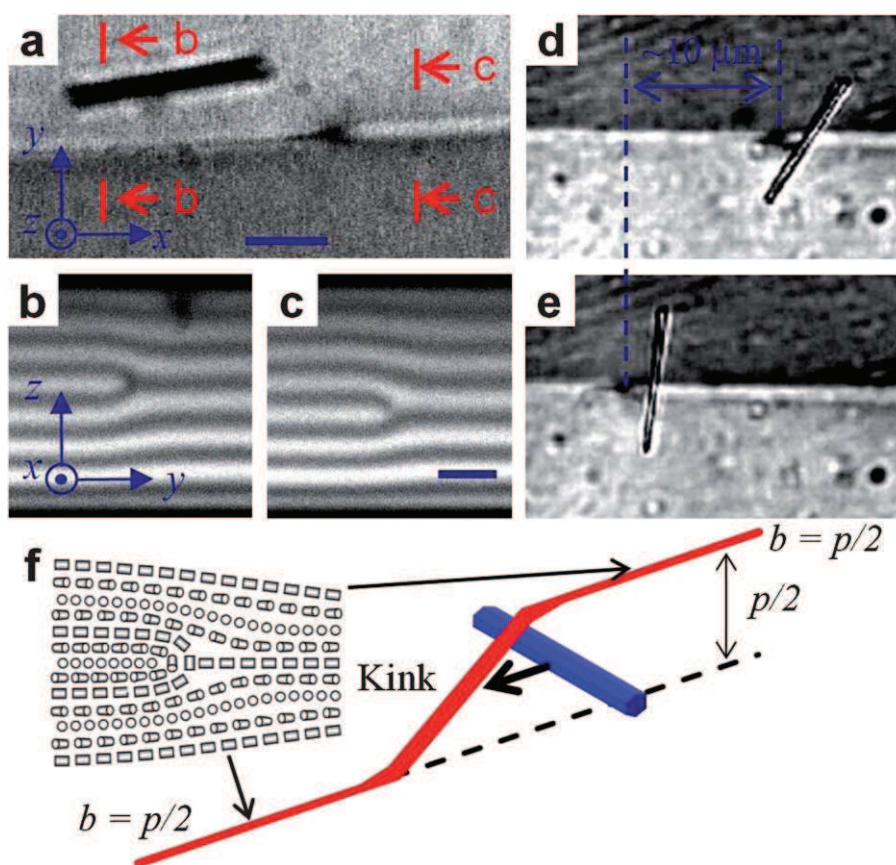


Fig. 7 Nanowire-controlled motion of a dislocation kink that shifts an edge dislocation across the layers. (a) FCPM in-plane cross-section showing a nanowire next to a kink of an elementary $b = p/2$ dislocation. (b and c) Confocal vertical cross-sections along the b - b and c - c lines [marked on the image in (a)] show the dislocation at different positions across the layers; the FCPM polarization is orthogonal to the images in (b) and (c). (d and e) Snapshots from a movie (Video S4†) showing that the dislocation kink is displaced along the edge dislocation as the nanowire is shifted to the left by use of optical traps. (f) Schematics of a kink of the manipulated $b = p/2$ dislocation; the inset shows the defect core structure of an edge dislocation. The scale bars in (a) and (c) are $5 \mu\text{m}$. Note that the optically manipulated nanowire visible in (d and e) is nearly orthogonal to the two fragments of the edge dislocation inter-connected by the dislocation kink because it aligns with the local director corresponding to its location across the vertical section of the sample (intermediate between the vertical positions of the edge dislocations), as schematically depicted in (f).

nonsingular disclinations in its core split into the $\lambda^{+1/2}\tau^{-1/2}$ pair. When the nanowire is placed on the λ -disclination side of the dislocation core (Fig. 4), the nanowire-defect interactions are negligible even at separations $\sim p$. This is an expected result as the elastic energy cost of introducing a nanowire barely perturbing local $\mathbf{n}(\mathbf{r})$ into the non-singular λ -disclination core with a continuous twist of $\mathbf{n}(\mathbf{r})$ is close to that of a uniform CLC. However, a nanowire initially positioned on the τ -disclination-side of the dislocation is strongly attracted to its core. For example, a nanowire at an initial vertical position across the cell about $p/4$ away from the τ -disclination aligned along the local director \mathbf{n} and perpendicular to the dislocation (Fig. 6a) escapes the optical traps due to the CLC-mediated attraction which results in its localization within the core parallel to the defect line (Video S2† and Fig. 6b). Separating the nanowire pinned to the dislocation core by means of optical manipulation is impossible, even when using two laser traps of power about 250 mW each. The τ -disclination line is rigidly pinned over the entire length of the nanowire and follows its rotational and translational motion (Fig. 6d and f). The free energy per unit length of such a disclination is $F_\tau = (\pi K/4)\ln[p/(2r_c)] + F_{\text{core}}$, where r_c , and F_{core} are the radius of the defect core and the defect core energy, respectively. Taking experimental parameters of $K = 6$ pN and $p = 5$ μm , as well as $F_{\text{core}} = \pi K/4$ estimated for an isotropic (melted) core of radius $r_c = 10$ nm, one finds $F_\tau \approx 30$ pN. Placing a nanowire into the defect lowers the elastic energy per unit length to $F_{\text{nw-defect}} = (\pi K/4)\ln[p/(2R)] \approx 10$ pN (assuming that the surface anchoring at the CLC-nanowire interface is weak tangential and that the effects of weak elastic distortions at the nanowire ends can be neglected). For a nanowire of length $l = 10$ μm and singular τ -disclinations, the nanowire-core elastic binding energy is $\sim 2 \times 10^{-16}$ J $\gg K_B T$. Consistent with this, we find that nanowires strongly attract and pin to all singular defect lines while aligned parallel to them but their interactions with the nonsingular λ -disclinations are negligible. The defect-pinned nanowire can be freely translated along the disclination using low-power laser tweezers. Other optical translations and rotations of the pinned nanowire result in stretching of the defect line (Fig. 6d and Video S3†). These experimental findings are consistent with the results of recent numerical studies³⁵ demonstrating that colloidal particles tend to localize into singular defect cores to reduce the free energy cost due to defect lines.

Optically manipulated nanowires can be used to control defects in a number of different ways. The climb motion of dislocations parallel to lamellae requires only consecutive twist deformations preserving defect core structure and, thus, can be achieved by the nanowire-assisted translation of defects in the plane of layers (Fig. 6). The so-called Peierls–Nabarro friction (associated with the transformation of a defect core) hinders dislocation glide across the layers, so that its glide motion can be implemented only *via* kinks.^{16,39} With an optically manipulated nanowire, we have translated kinks and anti-kinks along an edge dislocation while also probing $\mathbf{n}(\mathbf{r})$ (Fig. 7 and Video S4†). For example, we show that “pushing” a kink of height $p/2$ over distances more than an order of magnitude larger than p shifts an edge dislocation across the layers but keeps its core structure unchanged (Fig. 7b, c and f).

4. Conclusions

To conclude, optically manipulated nanowires with weak surface anchoring and faceted sidewalls allow for nondestructive imaging and non-contact control of structures and defects in anisotropic fluids, providing single-defect-level insights into properties and physics of phenomena associated with topological singularities. The demonstrated self-positioning and self-alignment of nanowires in singular defect cores may enable means for mass production of metamaterials *via* controlled nanopatterning of liquid crystals that have periodic lattices of topological defects in their ground states, such as blue phases and twist grain boundary phases.^{34,35,39} The demonstrated 3D imaging technique based on holographic optical manipulation may employ other modes of probing nanowire’s orientation, such as those based on scattering and fluorescence and a number of nonlinear optical processes.^{40–42} It can be extended to the use of a variety of other nanowires or nanorods, such as plasmonic gold or silver nanowires and fluorescent quantum rods, allowing for nanoscale spatial resolution.

Acknowledgements

This work was supported by the Renewable and Sustainable Energy Initiative and Innovation Initiative Seed Grant Programs of University of Colorado, International Institute for Complex Adaptive Matter, and by NSF grants DMR-0820579, DMR-0844115, DMR-0645461, and DMR-0847782. D.E. acknowledges the support of the Swedish Foundation for International Cooperation in Research and Higher Education. We thank Noel Clark, Jason Gray, Tom Lubensky, Chuck Rogers, Leo Radzihovsky, and Hideo Takezoe for discussions.

References

- 1 P. Schall, I. Cohen, D. A. Weitz and F. Spaepen, *Nature*, 2006, **440**, 319–323.
- 2 S. J. Woltman, D. G. Jay and G. P. Crawford, *Nat. Mater.*, 2007, **6**, 929–938.
- 3 C. L. van Oosten, C. W. M. Baastiansen and D. J. Broer, *Nat. Mater.*, 2009, **8**, 677–682.
- 4 M. J. Bowick, L. Chandar, E. A. Schiff and A. M. Srivastava, *Science*, 1994, **263**, 943–945.
- 5 I. Chuang, R. Durrer, N. Turok and B. Yurke, *Science*, 1991, **251**, 1336–1342.
- 6 M. C. Miguel, A. Vespignani, S. Zapperi, J. Weiss and J. R. Grasso, *Nature*, 2001, **410**, 667–671.
- 7 J. Li, K. J. Van Vliet, T. Zhu, S. Yip and S. Suresh, *Nature*, 2002, **418**, 307–310.
- 8 D. Mainprice, A. Tommasi, H. Couvy, P. Cordier and D. J. Frost, *Nature*, 2005, **433**, 731.
- 9 B. Freedman, G. Bartal, M. Segev, R. Lifshitz, D. N. Christodoulides and J. W. Fleischer, *Nature*, 2006, **440**, 1166–1169.
- 10 A. M. Alsayed, M. F. Islam, J. Zhang, P. J. Collings and A. G. Yodh, *Science*, 2005, **309**, 1207–1210.
- 11 Y. Ran, Y. Zhang and A. Vishwanath, *Nat. Phys.*, 2009, **5**, 298–303.
- 12 L. Ramos, M. Zapotocky, T. C. Lubensky and D. A. Weitz, *Phys. Rev. E: Stat., Nonlinear, Soft Matter Phys.*, 2002, **66**, 031711.
- 13 M. Zapotocky, L. Ramos, P. Poulin, T. C. Lubensky and D. A. Weitz, *Science*, 1999, **283**, 209–212.
- 14 P. Schall, I. Cohen, D. A. Weitz and F. Spaepen, *Science*, 2004, **305**, 1944–1948.
- 15 I. I. Smalyukh, Y. Lansac, N. A. Clark and R. Trivedi, *Nat. Mater.*, 2010, **9**, 139–145.
- 16 I. I. Smalyukh and O. D. Lavrentovich, *Phys. Rev. E: Stat., Nonlinear, Soft Matter Phys.*, 2002, **66**, 051703.

- 17 R. Holyst and P. Oswald, *Int. J. Mod. Phys. B*, 1995, **9**, 1515–1573.
- 18 I. I. Smalyukh and O. D. Lavrentovich, *Phys. Rev. Lett.*, 2003, **90**, 085503.
- 19 A. De Luca, V. Barna, T. J. Atherton, G. Carbone, M. E. Sousa and C. Rosenblatt, *Nat. Phys.*, 2008, **4**, 869–872.
- 20 I. I. Smalyukh, S. V. Shiyankovskii and O. D. Lavrentovich, *Chem. Phys. Lett.*, 2001, **336**, 88–96.
- 21 D. G. Grier, *Nature*, 2003, **424**, 810–816.
- 22 K. A. Bertness, A. Roshko, N. A. Sanford, J. M. Barker and A. V. Davydov, *J. Cryst. Growth*, 2006, **287**, 522–527.
- 23 C. P. Lapointe, T. G. Mason and I. I. Smalyukh, *Science*, 2009, **326**, 1083–1086.
- 24 Certain commercial materials are identified in this paper in only order to specify the experimental procedure adequately. Such identification implies neither recommendation or endorsement by the National Institute of Standards and Technology, nor that the materials identified are necessarily the best available for the purpose. The description of the nanowire growth characteristics is excluded from the copyright coverage.
- 25 S. Anand, R. P. Trivedi, G. Stockdale and I. I. Smalyukh, *Proc. SPIE*, 2009, **7232**, 723208.
- 26 F. Brochard and P.-G. de Gennes, *J. Phys.*, 1970, **31**, 691–708.
- 27 J. Rault, P. E. Cladis and J. P. Burger, *Phys. Lett.*, 1970, **32A**, 199–200.
- 28 S.-H. Chen and N. M. Amer, *Phys. Rev. Lett.*, 1983, **51**, 2298–2301.
- 29 J. Vicario, N. Katsonis, B. Serrano Ramon, C. W. M. Bastiaansen, D. J. Broer and B. L. Feringa-Pieranski, *Nature*, 2006, **440**, 163.
- 30 P. G. De Gennes and J. Prost, *The Physics of Liquid Crystals*, Oxford University Press, New York, 1995.
- 31 M. Škarabot and I. Muševič, *Soft Matter*, 2010, **6**, 5476–5481.
- 32 U. Tkalec, M. Škarabot and I. Musevic, *Soft Matter*, 2008, **4**, 2402.
- 33 D. Pires, J. P. Fleury and Y. Galerne, *Phys. Rev. Lett.*, 2007, **98**, 247801.
- 34 G. Cordoyiannisa, et al, *Liq. Cryst.*, 2010, **37**, 1419–1426.
- 35 M. Ravnik, G. P. Alexander, J. M. Yeomans and S. Žumer, *Proc. Natl. Acad. Sci. U. S. A.*, 2011, **108**, 5188.
- 36 M. Škarabot, M. Ravnik, S. Žumer, U. Tkalec, I. Poberaj, D. Babič and I. Muševič, *Phys. Rev. E: Stat., Nonlinear, Soft Matter Phys.*, 2008, **77**, 061706.
- 37 Q. Liu, Y. Cui, D. Gardner, X. Li, S. He and I. I. Smalyukh, *Nano Lett.*, 2010, **10**, 1347–1352.
- 38 C. D. Santangelo and R. D. Kamien, *Phys. Rev. Lett.*, 2003, **91**, 045506.
- 39 P. M. Chaikin and T. C. Lubensky, *Principles of Condensed Matter Physics*, Cambridge Univ. Press, Cambridge, 2000.
- 40 T. Lee, R. P. Trivedi and I. I. Smalyukh, *Opt. Lett.*, 2010, **35**, 3447–3449.
- 41 R. P. Trivedi, T. Lee, K. A. Bertness and I. I. Smalyukh, *Opt. Express*, 2010, **18**, 27658–27669.
- 42 R. P. Trivedi, D. Engström and I. I. Smalyukh, *J. Opt.*, 2011, **13**, 044001.

Supplementary Information

Three-dimensional imaging of liquid crystal structures and defects by means of holographic manipulation of colloidal nanowires with faceted sidewalls

David Engström,^{a,b} Rahul P. Trivedi,^{a,c} Martin Persson,^{a,b} Mattias Goksör,^b Kris A. Bertness,^d and Ivan I. Smalyukh^{a,c,e*}

^a*Department of Physics, University of Colorado, Boulder, Colorado 80309, USA*

^b*Department of Physics, University of Gothenburg, 412 96 Göteborg, Sweden*

^c*Liquid Crystal Materials Research Center, University of Colorado, Boulder, Colorado 80309, USA*

^d*National Institute of Standards and Technology, Boulder, Colorado 80305, USA*

^e*Renewable and Sustainable Energy Institute, University of Colorado, Boulder, Colorado 80309, USA*

* To whom correspondence should be addressed. E-mail: Ivan.Smalyukh@colorado.edu

Supplementary Methods

Nanorod preparation. The GaN nanorods are grown by molecular beam epitaxy under conditions of high substrate temperature (810-830 °C) and high nitrogen plasma flux at a chamber pressure of ~2.6 mPa. The nanorods nucleate spontaneously under these growth

conditions on thin AlN buffer layers on Si(111) substrates. The nanorod growth rates were 0.1-0.2 $\mu\text{m/h}$ and typical growth lengths were from 12 μm to 15 μm (varying from one part of the wafer to another). The dispersed nanorods used in this work typically break off with lengths of $\sim 10 \mu\text{m}$. Further details of the growth mechanism and conditions for the GaN nanorods have been reported elsewhere.^{1,2} The nanorods were doped with Si during growth such that a free carrier concentration between $3 \times 10^{17} \text{ cm}^{-3}$ and $1 \times 10^{18} \text{ cm}^{-3}$ was obtained. At these doping levels, the absorption coefficient is $\sim 80 \text{ cm}^{-1}$ at 1064 nm.³ The long axis of the nanorods follows the c-axis (0001) of their wurtzite crystal structure, with the sidewalls all being m-planes [(1 $\bar{1}$ 00) family], and thus they are hexagonal in cross-section. Nanorods grown using this method are defect-free monocrystals with interesting mechanical and optical properties.⁴⁻⁶

Supplementary References

1. Bertness K. A.; Roshko, A.; Sanford, N. A.; Barker, J. M.; Davydov, A. V. *J. Cryst. Growth*. **2006**, 287, 522-527.
2. Bertness, K. A.; Roshko, A.; Mansfield, L. M.; Harvey, T. E.; Sanford, N. A. *J. Cryst. Growth* **2008**, 310, 3154-3158.
3. Ambacher, O. *et al. Sol. State Commun.* **1996**, 97, 365-370.
4. Bertness, K. A. *et al. J. Electron. Mat.* **2006**, 35, 576-580.
5. Tanner, S. M.; Gray, J. M.; Rogers, C. T.; Bertness, K. A.; Sanford, N. A. *Appl. Phys. Lett.* **2007**, 91, 203117.
6. Schlager, J. B. *et al. J. Appl. Phys.* **2008**, 103, 124309.

Supplementary videos

Supplementary Video SV1. Controlling nanorod rotation using holographic optical tweezers. Two infrared optical traps (not visible) at the nanorod ends are used to rotate it by 360° . The rotated nanorod changes z -position, unlike the stationary nanorod seen on the right; the focusing plane is continuously adjusted to coincide with the manipulated nanorod. The video speed has been increased by a factor of two.

Supplementary Video SV2. Self-alignment and self-positioning of a nanorod along the singular τ -disclination in the core of a $b=p/2$ edge dislocation. Fragments of movies showing how two optical traps are used to place a nanorod about $p/4$ beneath a dislocation and then slowly rotate CCW towards the dislocation core. When at an angle of $\sim 45^\circ$ (after ~ 32 s into the movie), the nanorod escapes from the optical traps, self-rotates to become parallel to the τ -defect line, and is eventually “sucked” into the disclination.

Supplementary Video SV3. Nanorod-based manipulation of a defect line. Two optical traps moving in opposite directions rotate the nanorod, allowing manipulation of the defect line which follows the orientation of the nanorod. In the end of the movie (~ 6.5 into the movie) the two traps are blocked and the defect line relaxes back to a straight line. During the relaxation the nanorod is reoriented along with the defect line.

Supplementary Video SV4. Nanorod manipulating a $b=p/2$ dislocation kink. The dislocation kink is displaced by ~ 10 μm along the edge dislocation as the nanorod is shifted to the left by use of two optical traps.